

Supplementary information

**Topographic stress control on bedrock
landslide size**

In the format provided by the
authors and unedited

1
2 **Supplementary Materials for**
3

4 **Topographic stress control on bedrock landslide size**

5 Gen Li^{1,2} and Seulgi Moon¹
6

7 ¹Department of Earth, Planetary, and Space Sciences, University of California Los
8 Angeles, Los Angeles, California 90095, USA

9 ²Present address: Division of Geological and Planetary Sciences, California Institute
10 of Technology, Pasadena, California 91125, USA
11

12
13 **Contents:**

14 **Supplementary Text S1-S4**

15 S1. Landslide mapping, characterization, and distributions

16 S1.1 Landslide mapping procedure

17 S1.2 Bedrock landslide characterization

18 S1.3 Landslide area distributions and spatial locations
19

20 S2. Topographic stress calculation

21 S2.1 Ambient stress conditions and stress measurement datasets

22 S2.2 Topographic perturbation calculation and model configurations

23 S2.3 Model assumptions and discussion
24

25 S3. Quantification of potential controls on bedrock landslides

26 S3.1 Proxies for topographic stress

27 S3.2 Metrics for topography

28 S3.3 Proxies for seismic shaking

29 S3.4 Proxies for precipitation rate and variability
30

31 S4. Statistical analysis for comparing landslide metrics and potential controls
32
33

34 **Supplementary Figures 1-10**
35
36

37 **Supplementary Tables 1-4** (Uploaded as a separate excel file)

38 Table 1. Compilation of stress measurements near our study area

39 Table 2. Stress model parameter values used in this study.

40 Table 3. Correlation coefficient and *p*-value for landslide metrics and 14 potential
41 controls

42 Table 4. Proportion of bedrock landslides located in FP_{\max} higher than expected.
43

44 **S1. Landslide mapping, characterization, and distributions**

45 **S1.1 Landslide mapping procedure**

46 We constructed two landslide inventories, one for earthquake-induced landslides and
47 one for precipitation-induced landslides, using 0.5 m-resolution satellite images from
48 DigitalGlobe (WorldView and QuickBird). Landslide polygons were manually
49 delineated using ArcGIS based on distinct differences of spectral intensity between
50 landslides and surrounding vegetation. Specifically, for each landslide, we delineated
51 polygons separately for landslide scars (source) and deposition (runout) zones. The
52 high-resolution (0.5 m) satellite images allowed us to identify the boundary between
53 exposed bedrock surface and landslide deposit. This boundary was used to
54 differentiate the scar and deposition zones. Landslide deposits often contained
55 mixtures of granular materials with visible meter-sized boulders, showing different
56 brightness and textures compared to the scars, and the scar walls often have linear
57 features such as joints. We mapped the landslide scar and deposit as a whole polygon
58 and separated the polygon based on the scar-deposit boundary. The above-boundary
59 part is defined as the scar zone, and the below-boundary part is the deposition zone.
60 Our approach likely produced a minimum, conservative estimate for scar area due to
61 the possibility that deposits have obscured the bottom of the slip surface¹. In general,
62 our mapped scar areas correlated well with the entire mapped areas ($r = 0.90$,
63 $p < 0.0001$) and encompass on average 62% of entire landslide areas (Supplementary
64 Fig. 1e).

65

66

67 Since we were interested in the initial conditions of landslide failure, we focused on
68 the dimensions of landslide scars (e.g., area, width). Landslide scar area was
69 measured as the planar area of the delineated landslide scar polygon. Landslide depth
70 was derived from the measured landslide area based on an empirical area-volume
71 scaling relationship calibrated for our study region^{2,3}. Landslide scar width was
72 measured as the maximum horizontal distance perpendicular to the runout pathway,
73 which was independently measured from landslide scar area.

74

75 For the earthquake-induced landslide inventory, we mapped landslides with an area >
76 5,000 m² using satellite images from before and after the 2008 M_w 7.9 Wenchuan
77 earthquake. 2619 landslides were mapped within the six months following the
78 Wenchuan earthquake (June to December 2008, excluding the pre-Wenchuan
79 landslides). We attributed these landslides to be caused by the mainshock and
80 aftershocks of the Wenchuan earthquake. For the precipitation-induced landslide
81 inventory, we mapped 209 landslides with an area > 5,000 m² from satellite images in
82 2007, before the Wenchuan earthquake. We considered that these pre-2008 landslides
83 were likely triggered by precipitation-related effects. The recurrence interval of a
84 Wenchuan-like event in the Longmen Shan fault system is estimated to be around
85 500-4000 years⁴. The vegetation turnover time is typically ~30 years⁵, and there were
86 limited seismicity over a period of 30 – 100 years before the 2008 Wenchuan
87 earthquake in the study area. Two major $\sim M_w$ 7 events occurred in the century before

88 the Wenchuan earthquake in the eastern Tibetan region, the 1933 Diexi earthquake
89 and the 1976 Songpan-Pingwu earthquake^{6,7}, which were ~100 km and ~250 km away
90 from our study area, respectively. We expect that these two events have minimal
91 influences on our pre-2008 precipitation-induced landslide inventory due to following
92 reasons. The reconstructed peak ground acceleration (PGA) distribution of the
93 Songpan-Pingwu earthquake by the USGS Hazard Program
94 (<https://earthquake.usgs.gov/earthquakes/eventpage/usp0000j0p/shakemap/pga>)
95 suggests that this event caused a PGA of <0.05 g in our study area, much smaller than
96 the typical PGA magnitude (0.15-0.2 g) shown to trigger landslides^{4,8,9}. For the Diexi
97 event, a recent paleoseismological study showed that this earthquake had a rupture
98 length of around 30 km¹⁰, which did not propagate to our study area. The estimated
99 epicenter location is ~100 km away from our study area. Because previous studies
100 have shown that the areal density of earthquake-induced landslides decayed rapidly
101 within 40 km from the epicenter or seismogenic fault^{4,9,11,12}, we expect that these
102 earthquakes have limited influences on our mapped landslides.

103

104 Note that this earthquake-induced landslide inventory represents a new dataset based
105 on high-resolution images, which is different from previously published Wenchuan
106 earthquake-induced landslide inventories^{4,11-13}. Those previous Wenchuan landslide
107 inventories have not separated the scars and deposits, whereas our new inventories of
108 both precipitation-induced landslides and earthquake-induced landslides delineated
109 both entire landslide areas and scar areas.

110

111 **S1.2 Bedrock landslide characterization**

112 The major objective of our study is to evaluate the controls on the sizes of bedrock
113 landslides, which are thought to be controlled by mechanisms different from those
114 that control soil landslides¹⁴⁻¹⁶. Bedrock landslides tend to have greater areas and
115 deeper failure planes than shallow soil landslides that occur typically at soil-bedrock
116 boundaries¹⁵. In reality, a transition zone between soil and bedrock landslides appears
117 as a broad zone¹⁵, and we may not be able to completely separate them in our
118 inventories. Here, we illustrate how we determine the range of landslide areas that
119 separate bedrock landslides from soil landslides based on several prior studies.

120

121 A prior study³ conducted field surveys of earthquake-induced landslides following the
122 Wenchuan event and found that most landslides were bedrock landslides. This study³
123 reported measurements of the depths of 41 landslides in the field, with measured
124 depths varying from < 1 m to ~ 20 m and areas varying from $\sim 1,000$ m² to $\sim 300,000$
125 m². These measurements provide a locally calibrated scaling relationship between
126 landslide area and depth. A global compilation of soil and bedrock landslides¹⁵
127 showed a broad transition zone between soil and bedrock landslides. Most soil
128 landslides have areas $< 10,000$ m² and few soil landslides have areas close to $100,000$
129 m². The lower bound for the transition between soil/bedrock landslides to bedrock
130 landslides only is around $35,000$ m². We note that the global dataset contains soil
131 landslides from soil-mantled landscapes with low slope angles and thick soil¹⁵, thus

132 their inferred area to transition from soil/bedrock landslides to bedrock landslides
133 only likely represents an upper estimate for steep uplifting mountains like the
134 Longmen Shan.
135
136 Based on compilations of soil landslides from California and Switzerland, a recent
137 study¹⁶ estimated landslide thickness using landslide volume and geometry in
138 landscapes with steep slopes. They showed that landslide thicknesses scale with
139 hillslope gradients and are typically less than 3 m for areas with steep slopes
140 (gradient > 0.5)¹⁶. This estimate corresponds to a landslide area of ~6,000 m² using
141 the locally calibrated landslide area-depth scaling relationship in the Longmen Shan
142 region. This depth is comparable to one available measurement of soil thickness (~
143 1.8 m) in a steep granitic terrain in the eastern Tibetan mountains¹⁷, a setting similar
144 to our study area. Following these observations, we speculate that landslides with an
145 entire area greater than the range of 5,000 - 35,000 m², corresponding to a landslide
146 thickness of 2.9 - 6 m based on the local landslide area-depth scaling relationship,
147 likely separate bedrock landslides from soil landslides in our study area. We then
148 selected a landslide area of 20,000 m² (equivalent to a landslide depth of 5.9 m) as our
149 best estimate of the minimum area that separates soil and bedrock landslides.
150
151 For the following analysis, we used landslides with entire areas larger than 20,000 m²
152 as bedrock landslides. In total, we identified 861 Wenchuan earthquake-induced
153 bedrock landslides, and 121 precipitation-induced bedrock landslides before the

154 Wenchuan earthquake.

155

156 To examine the impact of choice for the minimum area, we performed sensitivity tests
157 using landslide areas that vary from $\sim 5,000$ to $35,000 \text{ m}^2$. We find that the
158 correlations between the maximum failure potential (FP_{\max}) and the 95th percentiles of
159 landslide scar areas do not change significantly depending on the choice of the
160 minimum area, showing consistently high and statistically significant weighted
161 correlation coefficients ($r_w = 0.85$ to 0.95 for earthquake-induced landslides, $r_w = 0.73$
162 to 0.79 for precipitation-induced landslides) (Supplementary Figs. 6c, d).

163

164 **S1.3 Landslide area distributions and spatial locations**

165 We examined the size-frequency distributions of scar areas of earthquake-induced and
166 precipitation-induced landslides using histograms and probability density plots
167 (Supplementary Fig. 1b). The probability density of landslide inventories for a given
168 area A_L , $p(A_L)$ is defined following ref¹⁸:

169

$$170 \quad p(A_L) = \frac{1}{N_{LT}} \frac{\delta N_L}{\delta A_L} \quad (\text{Eq. S1})$$

171

172 where δN_L is the number of landslides within an area bin between A_L and $A_L + \delta A_L$, and
173 N_{LT} is the total number of landslides in the inventory. The comparison of size-
174 frequency distributions of two inventories revealed that precipitation-induced
175 landslides tend to be larger than earthquake-induced landslides (Supplementary Figs.

176 1a, b).

177

178 In addition, we examined the locations of landslides relative to ridges and channels
179 and assessed whether landslide sizes differ depending on landscape positions
180 (Extended Data Fig. 1). Following the analysis in a previous work¹⁹, we calculated the
181 distance to ridge as the steepest decent distance from the highest point of a landslide
182 scar to the nearest ridgeline and the distance to channel as the steepest decent distance
183 from the lowest point of landslide scar to the nearest channel. The channels were
184 defined as topographic points with drainage area $> 1 \text{ km}^2$ ²⁰ and the ridgelines were
185 determined by extracting the channels from inverted digital elevation model (DEM)
186 data with visual examination and correction. These distances were normalized by the
187 total flow length of the hillslope to show relative positions with respect to ridge and
188 channel.

189

190 We found that bedrock landslides with large scar areas (e.g., $> 40,000 \text{ m}^2$) in both
191 landslide types tend to occur more in ridges, but some large landslides also occur in
192 other landscape positions. Fig. 1d shows that precipitation-induced landslides were
193 clustered in the E-W oriented ridge in the north of the catchment, while earthquake-
194 induced landslides tend to occur more broadly across the landscape. Such spatial
195 differences may be derived from the fact that earthquake-induced landslides were
196 more likely to occur at hillslopes that have not failed before by precipitation-induced
197 landslides. The long recurrence interval of Wenchuan-like events in this region (500-

198 4,000 yr)⁴ likely allowed ample time for seismically-failed landscapes to recover and
199 re-steepen for failure in future events. The exact timing of precipitation-induced
200 landslides clustered in the E-W oriented ridge in the north is not clear, whereas this
201 area features high steepness, high elevation, and high failure potential. We speculate
202 that those landslides in high elevations are likely affected by deep open-fracture zones
203 and triggered by precipitation-related factors. It is possible that the expected deep
204 open-fracture zones beneath the E-W oriented ridge in the north might promote
205 percolation of groundwater and increase pore pressure at deep depths²¹, which can
206 facilitate large hillslope failures. In addition, the previous study²² suggested that the
207 effective stress affected by groundwater flow may destabilize the lower part of
208 hillslopes, which can cause large failures propagating to the ridges. Future research
209 efforts are needed to fully understand the interplay among topographic stress, open
210 fractures, groundwater flow, and bedrock landslides.

211

212 **S2. Topographic stress calculation**

213 We calculated the subsurface stress fields beneath the actual three-dimensional
214 topography considering the ambient stress fields from gravitational stresses and
215 horizontal far-field stresses (assumed to be tectonically induced) and the topographic
216 perturbation of the ambient stress fields. We assumed the topographic surface as a
217 traction-free boundary formed by the removal of overburden within the body of rock
218 ²³⁻²⁵. The topographic perturbation on the ambient elastic stress field is calculated
219 using the boundary element model Poly3D²⁶. The topographic stress model used in

220 this study is explained in previous studies^{21,27,28}. Although our stress model is based
 221 on simple material properties (linear-elastic, homogeneous and isotropic rock) that are
 222 rare in natural settings, previous studies have shown that our model can be used to
 223 examine the influence of elastic stress fields on subsurface fractures and weathering,
 224 which can be obtained from geologic and geophysical datasets (e.g., seismic velocity,
 225 fracture observations from cores)^{21,27,28}.

226

227 Here, we present information on 1) ambient stress conditions and stress measurement
 228 datasets, 2) topographic perturbation calculation and stress model configuration, and
 229 3) assumptions and discussion of the stress model used in this study.

230

231 **S2.1 Ambient stress conditions and stress measurement datasets**

232 We describe the subsurface ambient stresses, which include gravitational stresses and
 233 horizontal far-field stresses, as depth-dependent linear functions:

234

$$235 \quad \sigma_H^a = -k_H \rho g z + \sigma_H^t \quad (\text{Eq. S2a})$$

$$236 \quad \sigma_h^a = -k_h \rho g z + \sigma_h^t \quad (\text{Eq. S2b})$$

$$237 \quad \sigma_v^a = -\rho g z \quad (\text{Eq. S2c})$$

$$238 \quad \sigma_{Hh}^a = \sigma_{Hv}^a = \sigma_{hv}^a = 0 \quad (\text{Eq. S2d})$$

239

240 where the subscripts H , h , and v denote the directions of the most compressive
 241 horizontal stress, the least compressive horizontal stress, and the vertical stress,

242 respectively. The superscripts a and t denote the ambient stress and constant
243 horizontal tectonic stress, respectively. ρ is rock density ($2,650 \text{ kg/m}^3$), g is
244 gravitational acceleration (9.8 m/s^2), z is the elevation above a reference point, and k
245 is the vertical gradient in horizontal stress normalized by the vertical gradient in
246 vertical stress. The double subscripts in Eq. S2d refer to the directions of shear
247 stresses, following the on-in convention. Compressive stresses are defined as positive.
248

249 The magnitudes, orientations, and vertical gradients of ambient stresses were
250 determined from a compilation of *in-situ* stress measurements from five sites in the
251 central Longmen Shan range (Supplementary Figs. 2, 3, Supplementary Table 1²⁹⁻³¹).
252 Those sites were within 50 km from the center of our modeling window within a
253 region bounded by the Maowen-Wenchuan fault in the north and the Yingxiu-
254 Beichuan fault in the south (Supplementary Fig. 2). In total, we have 24 *in-situ* stress
255 measurements, which include one overcoring and 23 hydraulic fracturing
256 measurements. Among them, there are 13 measurements (three sites) made before the
257 Wenchuan earthquake and eight measurements (two sites) from granite. The
258 measured depths ranged from 100 m to 800 m. We used 23 hydraulic fracturing
259 measurements to constraint the ambient stress condition because they are typically
260 more accurate than the overcoring method³².

261

262 We constrained the intermediate range of horizontal stress magnitudes and the vertical
263 gradients of ambient stresses based on the linear fit between depths and stress

264 measurements. 1σ residual uncertainties of the fit provide the constraint for the lower
265 and upper bounds of stress profiles (Supplementary Figs. 3a-b, Supplementary Table
266 2). The estimated σ_H^t was 6.8 ± 3.2 MPa, σ_h^t was 4.6 ± 1.9 MPa, and the average
267 direction of H was $S50^\circ E$. Because stress measurements made close to the surface can
268 be affected by topographic perturbations, the vertical gradients of ambient stresses are
269 most consistent with those from sufficiently deep (>300 m) depths. We used the stress
270 model results based on intermediate stress profiles, as shown by the solid lines in
271 Supplementary Figs. 3a, b, for our analysis in Fig. 2. The results of the sensitivity
272 tests based on the lower and upper bounds are shown in Supplementary Figs. 3c and e
273 and explained in detail in section S2.3. The parameter values used in the stress model
274 scenarios are shown in Supplementary Table 2. We assumed a Young's modulus of
275 50 GPa.

276

277 The estimated horizontal far-field stresses in this area suggest a moderate-to-strong
278 compressive tectonic setting. For reference, an earlier study reported $\sigma_H^t = 7\pm 10$ MPa
279 and $\sigma_h^t = 6\pm 8$ MPa in the eastern United States³³. Another study²¹ reported σ_H^t
280 ranges from 6.25 to 10 MPa and σ_h^t ranges from 3 to 4 MPa from borehole hydraulic
281 fracturing and overcoring measurements for their study sites in the eastern United
282 States with strong compression.

283

284 **S2.2 Topographic perturbation calculation and model configurations**

285 We calculate the stress perturbation caused by the topographic surface on ambient

286 stress fields using a boundary element model, Poly3D²⁶. To do this, we first used the
287 actual topographic surface and constructed boundary elements. We smoothed the
288 SRTM 90m DEM using a moving-average circular filter with a radius of 500 m,
289 which is about half of the regional hillslope length scale. This procedure removed
290 local irregularities and noise in the DEM, hence reducing numerical artifacts at
291 shallow depths²¹. We selected a total area of $\sim 1,600 \text{ km}^2$ ($40 \text{ km} \times 40 \text{ km}$), which
292 encompassed our immediate study site (525 km^2 , $25 \text{ km} \times 21 \text{ km}$), to account for
293 topographic perturbation from surrounding topography (Fig. 1). Then, we subtracted
294 the mean elevation from the smoothed DEM and tapered the edges of the modeled
295 window to zero elevation to ensure stress state equilibrium. We discretized this
296 topographic surface into a mesh of triangular elements using the 3D Move software
297 from Midland Valley Inc. The length of the triangular elements was $\sim 350 \text{ m}$ within
298 our study site and was gradually coarsened ($\sim 1500 \text{ m}$) outside of our study site. The
299 length 350 m is chosen so our large study area can be processed in a reasonable total
300 simulation time with a stress model that is computationally expensive and time-
301 consuming.

302

303 Then, we resolved the ambient stresses onto the plane of each triangular element and
304 subtracted those stresses from the zero-traction boundary condition. We used these
305 modified traction conditions as an input to Poly3D and calculated the displacements
306 on the surface elements that satisfy the modified traction conditions and elastic
307 equilibrium²⁶. Finally, we added the stress perturbation from displacements to the

308 ambient stresses to calculate the total stress field at observational points in the
309 subsurface. This total stress field is used to quantify the proxies for open-fracture
310 zones in the subsurface (e.g., FP_{500m}, LCS_{500m}, D_{10MPa}; see Methods). The
311 observational points were implemented as a three-dimensional matrix that covered a
312 volume of $\sim 21 \text{ km} \times 25 \text{ km} \times 6 \text{ km}$. The matrix is composed of 49 (E-W) \times 59 (N-S)
313 \times 119 (vertical) points, with a horizontal spacing of 440 m and a vertical spacing of
314 50 m.

315

316 **S2.3 Model assumptions and discussion**

317 Our topographic stress model assumes a simple mechanical property of rock and does
318 not calculate the influence of geologic structures or varying lithologies. Thus, we
319 modeled a region in a granitic terrain without active geologic structures within it (Fig.
320 1, Supplementary Fig. 2) and used ambient stress measurements from nearby sites.
321 However, it is possible that the compiled orientations and magnitudes for ambient
322 stress conditions may be affected by nearby geologic structures, lithologies, and the
323 timing of earthquakes. Among 24 measurements, 13 measurements (three sites) were
324 made before the Wenchuan earthquake. Eight measurements (two sites) were from
325 areas of granitic lithology. Previous studies show that major earthquakes such as the
326 2008 Wenchuan event may induce transient changes in stress magnitudes and
327 orientations after a few months to a few years^{34,35,30}. A local study³⁰ showed a 23-
328 29% decrease in stress magnitudes in the northern section of the Longmen Shan,
329 measured within two months after the Wenchuan earthquake. The stress

330 measurements from our site, in the middle section of the Longmen Shan, are
331 somewhat more compressive after the Wenchuan Earthquakes (Supplementary Figs.
332 3a, b). However, the lack of data from the same locations, lithologies, and
333 measurement depths precludes any strong conclusions. The H orientations are
334 consistently NW-SE before and after the Wenchuan earthquake, except for one
335 overcoring measurement from very close to the surface (20 m depth; N19E).
336
337 Despite the differences in site locations, lithologies, and the timing of measurements
338 relative to the Wenchuan earthquake, the overall trends in stress magnitude
339 measurements are relatively consistent (Supplementary Figs. 3a, b). The potential
340 ranges of *in-situ* stress measurements from nearby sites allow us to examine the
341 uncertainties of the total stress field. In addition to the stress model that used the best-
342 fit depth profiles of most and least compressive horizontal stresses, we perform
343 sensitivity tests that used the $\pm 1 \sigma$ range of the fit (Supplementary Table 2). We
344 showed the correlation coefficients between the 95th percentiles of landslide scar areas
345 and FP_{\max} based on these additional model scenarios in Supplementary Figs. 3c-e. We
346 found consistent results of strong correlations (weighted correlation coefficients $r_w =$
347 0.76, 0.92, and 0.90 for earthquake-induced landslides and $r_w = 0.76, 0.75,$ and 0.79
348 for precipitation-induced landslides) for the lower-bound, intermediate, and upper-
349 bound scenarios of the depth profiles of stress magnitudes, respectively. This test
350 indicates that the controls of topographic stress on bedrock landslide size are robust
351 and insensitive to the estimated uncertainties in the ambient stress measurements.

352

353 **S3. Quantification of potential controls on bedrock landslides**

354 We examined various potential controls of bedrock landslide magnitude and occurrence.

355 We consider the controls of 1) the extent of open-fracture zones induced by topographic
356 stress, 2) topography, 3) seismic shaking from the Wenchuan earthquake, and 4)
357 precipitation rate and variability. In total, we calculate maximum, minimum, and mean
358 values of 14 metrics and proxies, which include three proxies for topographic stress,
359 five metrics for topography, three proxies for seismic shaking, and three proxies for
360 precipitation. Below is a detailed explanation for the quantification of those controls.

361

362 **S3.1 Proxies for topographic stress**

363 We calculated three proxies to represent the influences of topographic stress in the
364 extent of open-fracture zones. Based on modeled total stress fields, we calculate three
365 proxies, the maximum value of failure potential at 500 m below the surface (FP_{max}), the
366 depth at which the least compressive stress = 10 MPa ($D_{10\text{ MPa}}$), and the least
367 compressive stress at 500 m below the surface (LCS_{500m}).

368

369 The choice of 500 m depth is related to the elemental length scale of the stress model
370 (~ 350 m triangle mesh size), the resolution of the original DEM (90 m), and the length-
371 scale of the DEM smoothing window (a radius of 500 m) to create meshes for stress
372 modeling. The large length scale of 100s of meters is inevitable due to the unavailability
373 of high-resolution, meter-scale DEM data and high computational cost for the large,

374 landscape-scale model. Although stress proxies at ~500 m depth may not be directly
375 used to predict failure planes and there are limitations to quantifying stress proxies at
376 depths close to that of landslide here (10s of meters), we think that the stress proxies at
377 500 m beneath the surface still provide a meaningful characterization of open-fracture
378 zones in the shallow subsurface of mountain ranges due to the following reasons.

379

380 First, the 500 m depth is comparable to or smaller than the vertical relief of hillslopes
381 in the study area. Previous studies have shown that the characteristic length-scales of
382 planar hillslopes in the study area is $\sim 1 \text{ km}^{20,36}$ and the hillslope of this region is steep ($>$
383 30°). Considering these facts, the vertical relief of the hillslope will be $> 500 \text{ m}$. Since
384 a 500 m depth is comparable to or smaller than the magnitude of topographic
385 variations, stress proxies at 500 m beneath the surface will capture the perturbations
386 induced by the typical 1 km-scale hillslopes in the landscape.

387

388 Second, there are spatial correlations between FP values at different depths, suggesting
389 that stress proxies at 500 m can be used to infer the locations of high FP at shallow
390 depths of 100s m beneath surface. The comparison among $\text{FP}_{500\text{m}}$, $\text{FP}_{1000\text{m}}$, and
391 $\text{FP}_{1500\text{m}}$ show that the influence of topographic perturbation on stress fields is evident
392 at 500 m and gradually disappears toward deeper depths (Supplementary Figs. 4g-i).
393 We expect that the general patterns of high FP due to 100s m scale landscapes (e.g.,
394 ridges) will be similar to those at shallow depths of 100s m beneath surface.

395

396 Third, a recent study based on stress modeling and fracture observation from deep
397 boreholes showed that present-day stress fields affected by surficial conditions and pore
398 pressure can influence fracture openness to depths of 500 m even in low
399 relief landscapes such as Sweden²⁸. Considering the significant topographic variation
400 and the measured strong horizontal compression at our study site, topographic stress
401 may also contribute to the reactivation and generation of open fractures to depths of
402 100s of meters or deeper here. In fact, previous studies reported pervasive and well-
403 developed fractures on surface outcrops and in a 185 m-deep borehole from nearby
404 areas²⁹. When high-resolution DEMs and stress modeling become available, we can
405 assess the impact of topographic stress variations from 10 m-scale landforms on
406 landslides, in addition to the impact of 100 – 1000 m scale landforms that we have
407 examined in this study.

408

409 **S3.2 Metrics for topography**

410 We calculated topographic metrics of hillslope gradient, local relief, elevation,
411 distance to channel, and mean negative curvature. We used the 90 m-resolution void-
412 filled SRTM DEM from the USGS EarthExplorer platform
413 (<https://earthexplorer.usgs.gov/>). Hillslope gradient was calculated using the slope
414 function in ArcGIS that fits a plane to a 3×3 cell matrix and chooses the steepest
415 descent along the plane from the central cell. Local relief was calculated as the range
416 of elevation within a 1 km-radius circular window. The length scale of 1 km
417 corresponds to the planar hillslope length observed in the study area^{20,36}. The distance

418 to channel is calculated as the steepest descent distance to the channel for all points
419 within landslide scar, as described earlier. Topographic curvature was calculated from
420 a smoothed DEM using a moving-average filter with a 500 m-radius window (half of
421 the hillslope length scale) that was also used for our topographic stress model. The
422 curvature from the smoothed DEM will be less affected by small-scale topographic
423 variations and hence provide information of the overall landscape such as the position
424 of ridges and valleys^{21,27}. Two components of curvature, profile, and planform
425 curvature were calculated along and perpendicular to the downslope direction. For
426 each DEM grid point, the mean curvature was calculated as the average of the profile
427 and planform curvatures²⁷. In this study, the topographic curvature was calculated as
428 the negative mean curvature. In this context, a negative curvature generally
429 corresponds to topographic ridges, whereas a positive curvature corresponds to
430 topographic valleys.

431

432 **S3.3 Proxies for seismic shaking**

433 We calculated three proxies that represent the magnitude of seismic shaking from the
434 Wenchuan earthquake, which may influence the size and occurrence of earthquake-
435 induced landslides. We used peak ground acceleration (PGA) data from the
436 ShakeMap produced by the USGS Earthquake Hazard Program
437 (<https://earthquake.usgs.gov/earthquakes/eventpage/usp000g650/executive>). We also
438 estimated an improved PGA corrected for the topographic amplification effect,
439 following the procedure of an earlier study³⁷. This study revised PGA estimates based

440 on the large-scale topographic curvature (hereafter, PGA corrected for amplification).
441 In short, this study³⁷ found empirical correlations between ground motions from three-
442 dimensional earthquake simulations and topographic curvature smoothed over a
443 characteristic length defined by half of the wavelength of S-waves. This approach has
444 been used to infer seismic amplification across a hillslope ridge in Taiwan³⁸. In our
445 study area, the magnitude of PGA is comparable to the magnitude of pseudo-spectral
446 acceleration (PSA) at a period of one second which was also provided by the USGS
447 Hazard Program
448 (<https://earthquake.usgs.gov/earthquakes/eventpage/usp000g650/executive>). Thus, we
449 used 1 s to calculate a characteristic wavelength using an S-wave velocity of 3,000 m
450 s⁻¹, which was determined from body wave seismic tomography in the Longmen Shan
451 region using data from a local seismic network³⁹. In addition, we calculate the
452 distance from the centroid points of landslide scars to the Yingxiu-Beichuan fault⁴⁰,
453 the major ruptured fault in our study area during the Wenchuan earthquake. The
454 distance to this fault was shown to be one of the major controls of landslide density
455 (landslide area per unit area or landslide number per unit area) following the
456 Wenchuan earthquake^{11,12}.

457

458 **S3.4 Proxies for precipitation rate and variability**

459 We calculated three precipitation proxies to represent the spatial distribution of
460 precipitation rate and variability that can influence the size and occurrence of
461 precipitation-induced landslides. Specifically, within each landslide scar zone, we

462 calculated the mean annual precipitation rates and 90th percentiles of precipitation
463 magnitudes using the Tropical Rainfall Measuring Mission precipitation
464 measurements (TRMM data product 2B31) averaged from 1998 to 2009⁴¹. Due to the
465 low resolution of the TRMM dataset (~ 2600 m), we only used the mean value for
466 each landslide.

467

468 In addition, we calculated a Slope Instability Proxy (*SIP*) to assess the propensity of
469 precipitation-induced landslides that are affected by both topographic slope and
470 increased pore-pressure due to a convergence of subsurface hydrology. We followed
471 the approaches of Montgomery and Dietrich (1994)⁴², in which the proxy is based on
472 an infinite slope stability model for a cohesionless frictional material coupled to a
473 steady-state hydrologic model for subsurface groundwater flow. This proxy is
474 typically used to assess the propensity of shallow landslides but has also been used for
475 bedrock landslides before^{43,44}. *SIP* is calculated using Eq. (S3):

476

$$SIP = \frac{\tan \theta}{\tan \varphi} \left(1 - W \frac{\rho_w}{\rho_s} \right)^{-1} \quad (\text{Eq. S3})$$

477

478

479 where θ is the local hillslope gradient, φ is the internal friction angle, ρ_s is the bulk
480 density of saturated hillslope material, ρ_w is the density of water, and W is the wetness
481 index representing the ratio between the local hydraulic flux at a given steady state
482 rainfall amount versus that at soil profile saturation. The wetness index W is
483 calculated as:

484

485

$$W = qA/(bT\sin\theta) \quad (\text{Eq. S4})$$

486

487 where q is the rainfall rate, A is the upstream contributing area over the contour length

488 b , and T is the soil transmissivity at saturation. The value of W is set to vary from 0 to

489 1, representing conditions from unsaturated to completely saturated, respectively.

490 Generally, the steep slopes that are affected by the increased pore-pressure will have

491 high SIP values, which represent a greater propensity for landsliding.

492

493 We calculated W and SIP assuming spatially uniform T ($3 \times 10^{-4} \text{ m}^2/\text{s}$), ρ_w (1,000

494 kg/m^3), ρ_s (2,000 kg/m^3), and ϕ (45°). For q , we used mean annual precipitation

495 derived from TRMM data product 2B31⁴¹. Note that we used a density of wet soil

496 instead of a density for saturated rock. The use of a different density changes the

497 magnitudes of SIP , but the spatial patterns of SIP are similar. We selected the T value

498 of $3 \times 10^{-4} \text{ m}^2/\text{s}$, which show large spatial variations of W . We calculated SIP for each

499 grid point on a hillslope with an upstream area $< 1 \text{ km}^2$ and obtained the maximum

500 and mean SIP value within each landslide polygon.

501

502 **S4. Statistical analysis for comparing landslide metrics and potential controls**

503 To compare the sizes, abundances, and locations of bedrock landslides and the 14

504 controls of topographic stress, topography, seismic shaking, and precipitation, we use

505 three approaches that are based on 1) binning of landslides based on the ranges of

506 potential controls, 2) segregating the study area to $2 \text{ km} \times 2 \text{ km}$ grids, and 3) all
507 landslide populations.

508

509 First, we grouped all bedrock landslides into 16 bins based on the ranges of potential
510 controls for both earthquake-induced and precipitation-induced landslides. Then, we
511 selected the 95th percentile of landslide area to represent large bedrock landslides and
512 defined the associated uncertainties as the 90th and 100th percentiles for each bin. The
513 16 bins will have on average $\sim 6\%$ of the total landslide count in each bin. We then
514 used the results from the bins that contain more than 3% of the total bedrock landslide
515 count (more than 50% of the expected average percent) to perform a regression with
516 potential controls. This criterion ensured that there were at least 4 precipitation-
517 induced landslides for each bin.

518

519 We examined the correlations between the 95th percentiles of scar areas and the 14
520 controls of stress, topography, seismic shaking, and precipitation for each landslide
521 (Figs. 2-4). We compared the 95th percentile of scar areas with both maximum and
522 mean values of the interested controls within each landslide scar zone. Although we
523 focused on the large bedrock landslides, we also examined the correlations between
524 the 50th percentile of scar areas and potential controls (Supplementary Fig. S5). We
525 reported the correlation coefficients (r_w), weighted by the percentage of landslide
526 counts, in each bin and the p -values for linear regressions between the different
527 metrics for landslide sizes and the various controls in Supplementary Table 3.

528

529 To examine the influences of the choice of the percentile of landslide sizes within a
530 given range of FP_{max} in Fig. 2, we performed a sensitivity analysis to examine how
531 statistical measures change with the choice of percentiles varying from 10th and 100th
532 (Supplementary Figs. S6a, b). We found that higher percentiles (i.e. larger landslides
533 were targeted) produce a stronger and more significant correlation between landslide
534 area and FP_{max} .

535

536 Second, we used a grid-based analysis to quantify landslide areal density and to
537 examine the potential controls on landslide occurrences. We segregated our study area
538 into a matrix of 130 (2 km × 2 km) grids. We quantified the areal density of landslides
539 in each 2 km × 2 km grid as the sum of landslide area (including both scar and deposit
540 area) divided by the total area of each grid (i.e., 4 km²). We then compared the
541 landslide areal density with the mean values of the 14 controls within the grid. This
542 grid-based analysis allows us to differentiate the controls of landslide areas (e.g., 50th
543 and 95th percentile) and occurrences (e.g., areal density). The landslide areas and areal
544 densities are inter-correlated to some extent (Supplementary Fig. 8). The correlation
545 between areal density and 95th percentile area is somewhat expected because large
546 landslides make a major contribution to the total landslide area. However, there is
547 appreciable scatter in the relationships among 50th and 95th percentile areas and areal
548 density, which may indicate a potential for different controls of landslide occurrences
549 and magnitudes.

550

551 Third, there are some extents of covariations between topographic stress proxies and
552 certain proxies (e.g. spatial covariations between mean negative curvature, failure
553 potential, and distance to channel for all DEM points, Supplementary Fig. 10). Here
554 we examined the covariations between topographic stress proxies and other potential
555 controls and assessed the relative importance of topographic stress controls. Based on
556 the bin-based analysis, we showed that only stress proxies show strong correlations
557 with the 95th percentile of landslide areas for both earthquake-induced and
558 precipitation-induced landslides. However, we also identified a few controls other
559 than stress proxies that showed good correlations with the 95th percentile of
560 earthquake- and precipitation-induced landslides, separately. To examine the
561 influence of the covariation between stress proxies and other controls, we plotted
562 FP_{\max} and other potential proxies and metrics from all mapped landslides. Then, we
563 showed landslide scar areas using circle symbols whose diameters are proportional to
564 scar areas (Fig. 5).

565

566 We found potential covariations between FP_{\max} and certain controls (e.g., gradient,
567 elevation, and curvature). Some degree of covariation is expected due to the
568 involvement of topography in subsurface stress perturbation, slope stability, and
569 seismic amplification. However, we find that although some large landslides occur in
570 high values of both FP_{\max} and other controls, a noticeable amount of landslides also
571 occur in locations with high FP_{\max} and a varying range of other controls. Notably, we

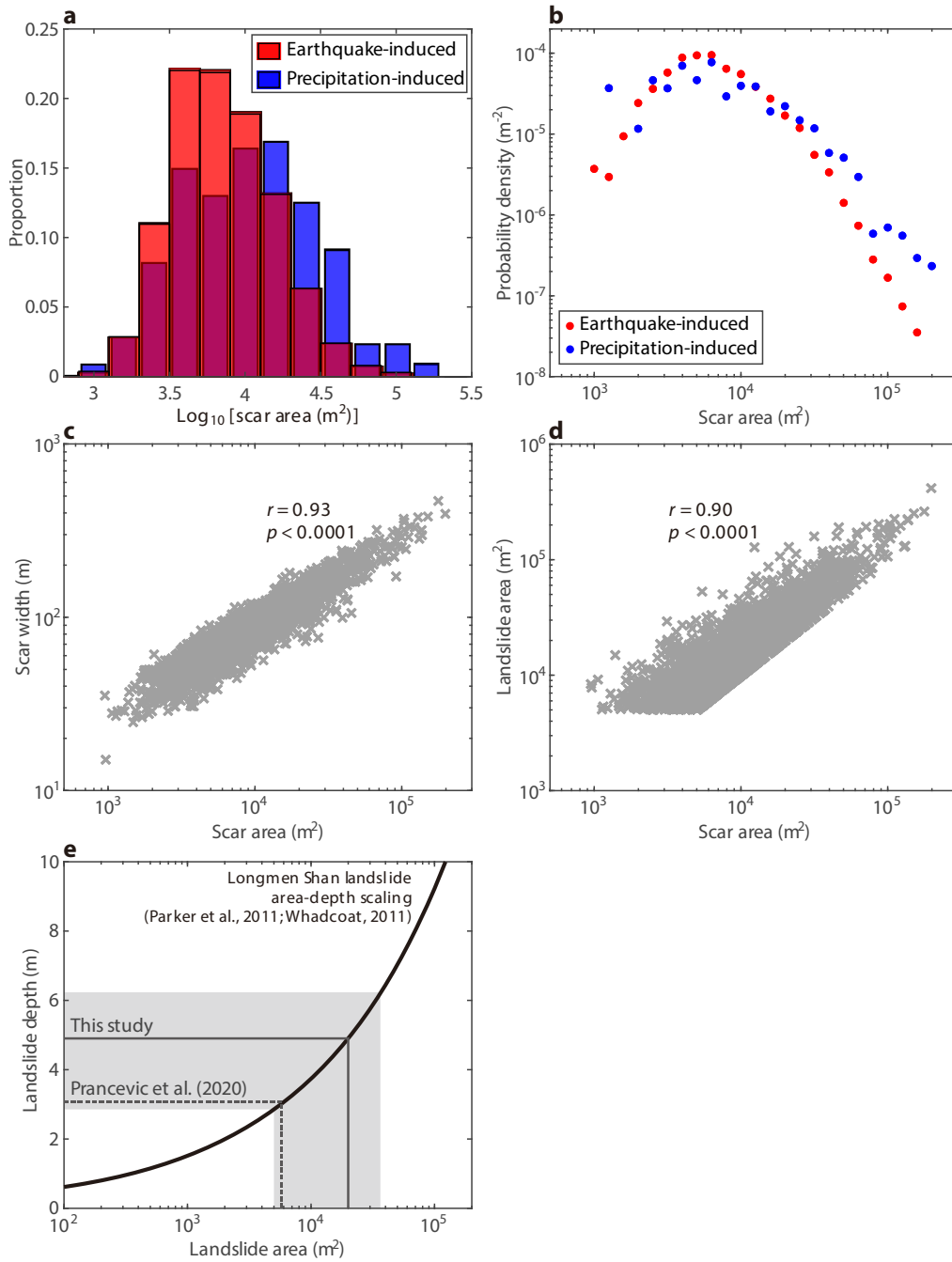
572 find that large bedrock landslides with scar areas $> 40,000$ to $>100,000 \text{ m}^2$ tend to
573 occur more where FP_{\max} exceed 0.4, and a majority ($\geq 50\%$) of those large bedrock
574 landslides persistently occur in FP_{\max} domains higher than that expected from the
575 regression line based on all landslides. We quantified the percentages of bedrock
576 landslides with FP_{\max} higher than the regression for varying sizes from $> 40,000$
577 to $>100,000 \text{ m}^2$ (Table S4). These observations indicate that the FP_{\max} controls on
578 landslide sizes are robust and evident across a varying range of other controls.

579

580

581

582 **Supplementary Figures**



583

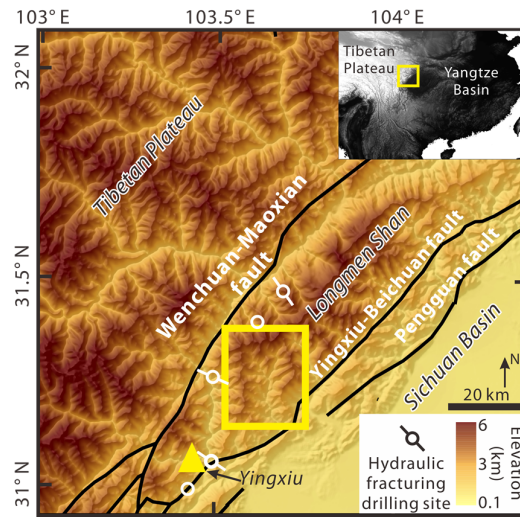
584

585 **Supplementary Figure 1.** Characterization of the sizes of the two landslide

586 inventories constructed in this study: **(a)** histograms and **(b)** probability density

587 distributions of scar areas for earthquake-induced (red) and precipitation-induced
588 (blue) landslides; correlations between scar area and (c) scar width and (d) entire
589 areas for all landslides; and (e) a Longmen Shan local landslide area-depth empirical
590 scaling relationship^{2,3}. The scaling relationship is based on measurements of 41
591 landslides (with 36 bedrock landslides and five soil landslides) following the
592 Wenchuan earthquake. The shaded area indicates our assumed ranges of areas that
593 separate soil and bedrock landslides in the study area. The dashed line indicates a
594 maximum soil thickness inferred from a gradient-based relationship for soil landslides
595 in California and Switzerland¹⁶. The solid line indicates our adopted area of 20,000m²
596 that separates soil and bedrock landslides. Note a local measurement¹⁷ suggests a soil
597 thickness of ~1.8 m in a steep granitic terrain in the eastern Tibetan mountainous
598 region, a setting similar to our study area.
599

600



601

602

603 **Supplementary Figure 2.** Elevation map of the Longmen Shan range. The yellow-

604 outlined box shows the domain of the stress model and the inset map at the upper

605 right shows the location of the study area in regional context bounded by the

606 Wenchuan-Maoxian fault and Yingxiu-Beichuan fault⁴⁰. Circles show the locations of

607 drilling sites for *in-situ* stress measurements with the lines denoting the orientation of

608 most compressive horizontal stress²⁹⁻³¹. Yellow triangle shows the location of Yingxiu

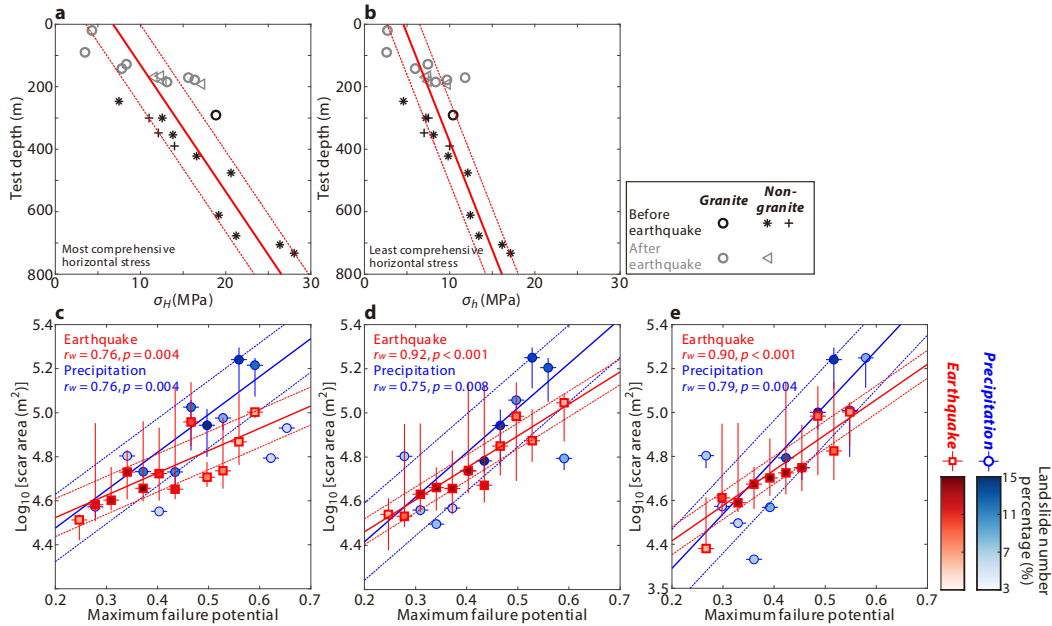
609 city.

610

611

612

613



614

615

616 **Supplementary Figure 3. (a, b)** Compilation of stress measurements near our study

617 area and **(c, d, f)** correlations between landslide scar area and maximum failure

618 potential (FP_{\max}) from different ambient horizontal stress conditions. **(a)** Most

619 compressive horizontal stress and **(b)** least compressive horizontal stress are shown

620 with measurement depths. Black and gray symbols represent measurements made

621 before and after the Wenchuan earthquake. Circle, star, cross, and left-pointing

622 triangle symbols represent measurements from granite, argillaceous siltstone and

623 sandy mudstone, sandstone, and phyllite, respectively. The solid lines show the depth

624 profiles of ambient stress conditions from linear least squares fits, and dotted lines

625 show the residuals of the fits (1σ errors). The compiled stress measurement data and

626 the constraint ambient stress condition used in the stress models are presented in

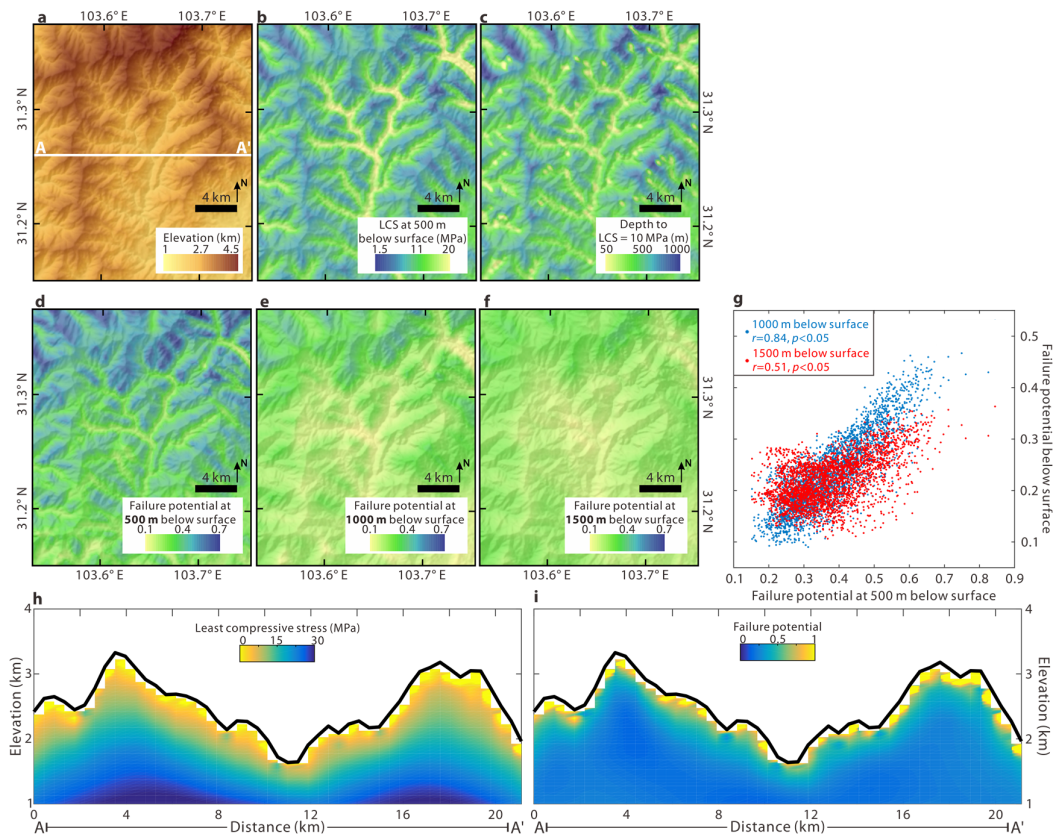
627 Supplementary Tables 1 and 2, respectively. The results of comparison between

628 landslide scar area and maximum failure potential (FP_{max}) based on ambient stress
629 conditions, defined by lower, intermediate, and upper range in **(a, b)** are shown in **(c,**
630 **d, e)**. Red and blue symbols and lines are results for bedrock landslides induced by
631 earthquakes and precipitation, respectively. The explanation for the symbols, colors,
632 and lines for **(c-e)** are the same as Fig. 2c.

633

634

635



637

638

639 **Supplementary Figure 4.** Stress model domain and results. (a) Digital elevation map
 640 of our topographic stress model domain and spatial distribution of (b) least
 641 compressive stress at 500 m below the surface, (c) the depth at which the least
 642 compressive stress = 10 MPa, and failure potential calculated at (d) 500 m, (e) 1000
 643 m, and (f) 1500 m below the surface. The ambient stress conditions used in this figure
 644 are shown in the solid red line in Supplementary Figs. 2a, b. (g) Comparison between
 645 failure potential at 500 m below the surface versus failure potential at 1000 m (blue
 646 dots) and 1500 m (red dots) below the surface, shown in blue and red dots, for all
 647 pixels within the study area. A two-dimensional vertical transect for modeled (h) least

648 compressive stress and (i) failure potential along the A-A' profile shown as a white
649 line in (a).

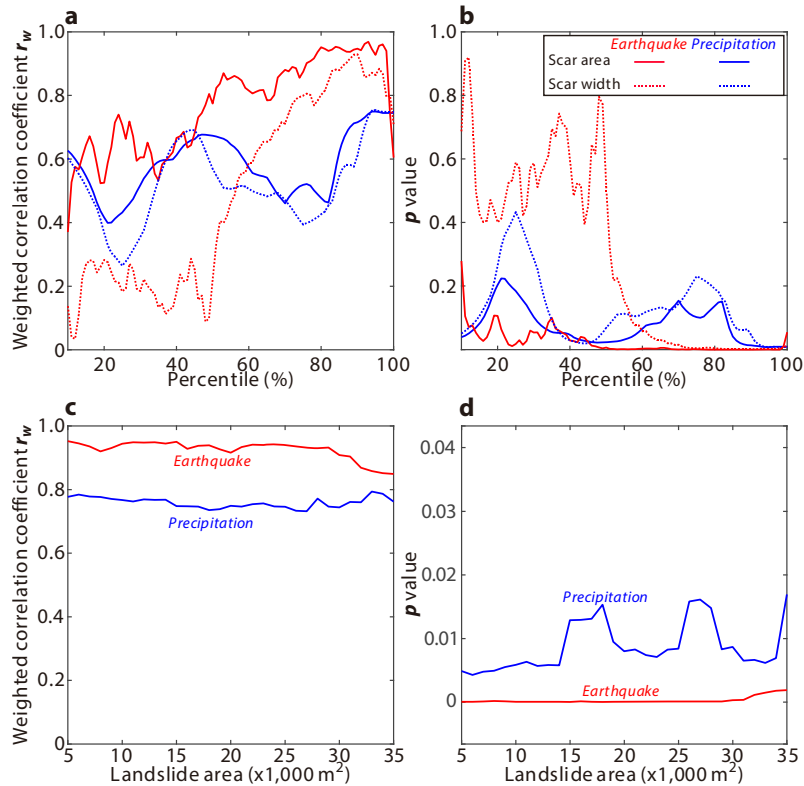
650

653 (FP_{max}) versus landslide scar width, **(d-f)** maximum failure potential (FP_{max}) versus
654 landslide entire areas, **(g-i)** maximum depth at which the least compressive stress = 10
655 MPa versus scar areas **(j-l)** minimum least compressive stress at 500 m below the
656 surface versus scar areas, and between **(m-o)** maximum failure potential versus scar
657 areas. The explanation for the symbols, colors, and lines are the same as Fig. 2.
658 Bedrock landslides induced by **(a, d, g, j, m)** earthquake, **(b, e, h, k, n)** precipitation,
659 and **(c, f, i, l, o)** both are shown. Small gray circles show all bedrock landslides whose
660 areas are greater than 20,000 m². Large colored symbols in **(a-l)** and **(m-o)** represent
661 the 95th and 50th percentile of scar areas for each bin, respectively. Vertical error bars
662 in **(a-l)** and **(m-o)** indicate 90th-100th and 45th-55th percentiles. The solid line
663 represents the fit between 95th or 50th percentile of scar area and FP_{max}, and the dashed
664 lines show the range of uncertainties based on the weighted root-mean-square error
665 (RMSE). The explanation for the symbols and colors is the same as Fig. 2.

666

667

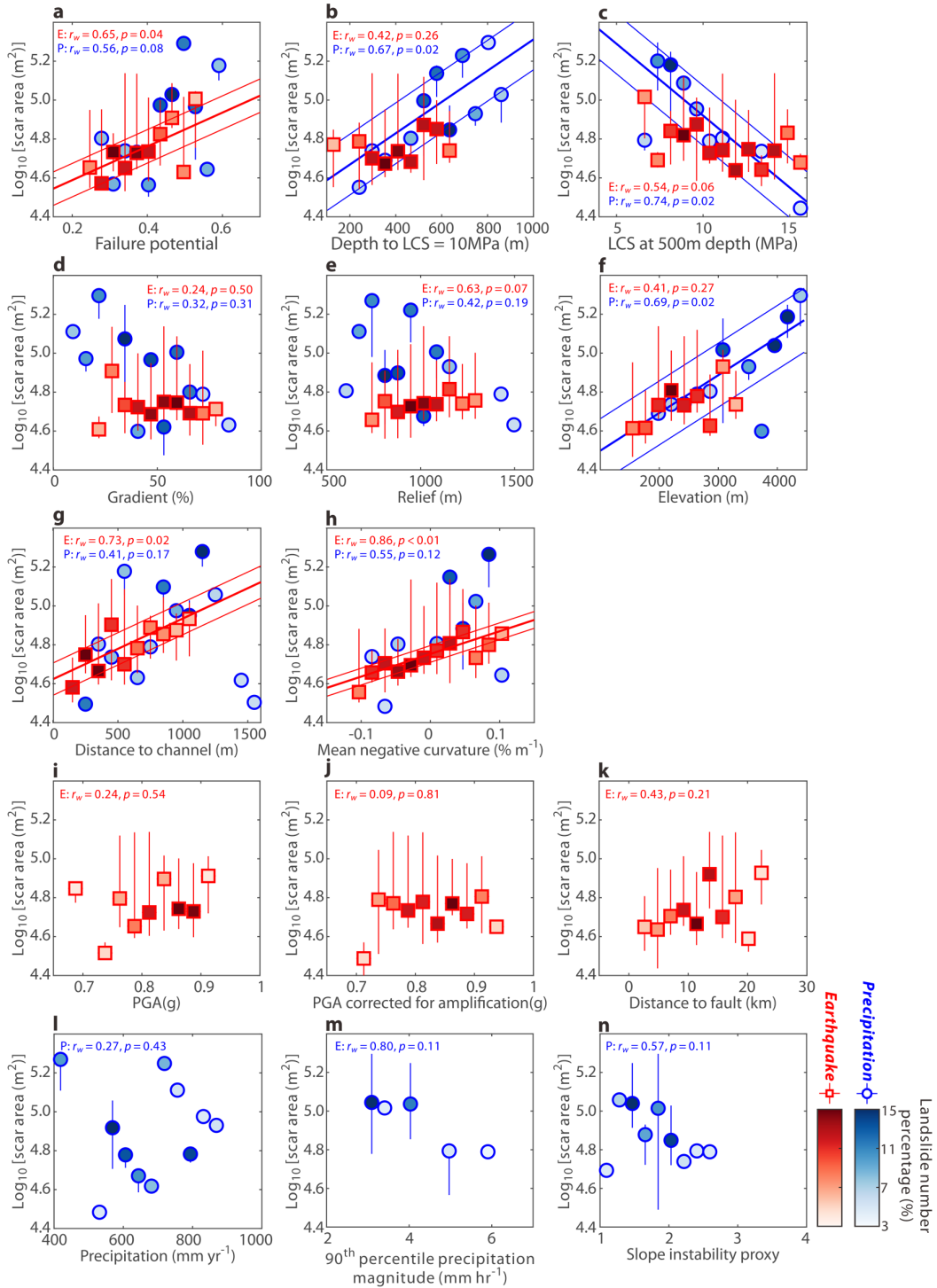
668



670

671

672 **Supplementary Figure 6.** Sensitivity analysis to examine how (a, c) weighted
 673 correlation coefficient, and (b, d) p -value vary with the choice of (a, b) percentile of
 674 landslide areas within a given range of FP_{max} and (a, b) the minimum area to separate
 675 bedrock landslides from soil landslides in Fig. 2. The correlations are statistically
 676 significant when using the upper 20 % of bedrock landslides areas from both
 677 earthquake-induced and precipitation-induced landslides. As the chosen percentile
 678 approaches 100%, statistical metrics are affected by a few maxima values and diverge
 679 from the general trends. In addition, there are strong, statistically significant
 680 correlations (p -value < 0.05) between FP_{max} and the 95th percentile area of bedrock
 681 landslides when using minimum areas varying from 5,000 to 35,000 m².



683

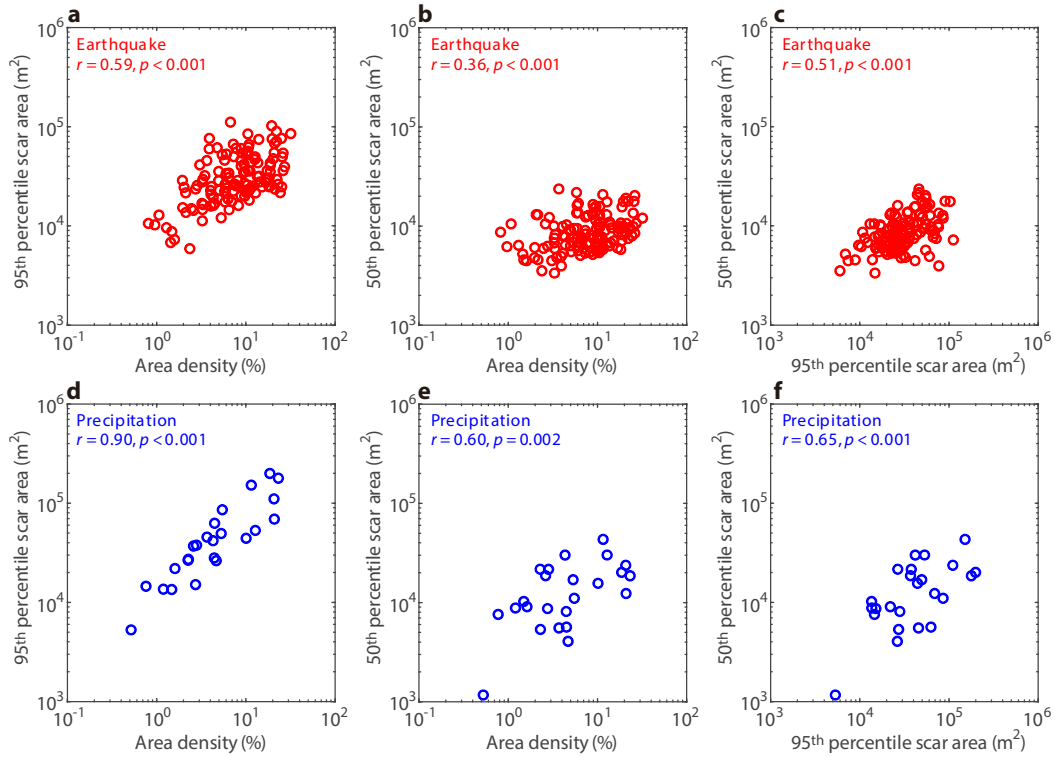
684

685 **Supplementary Figure 7.** Comparison between bedrock landslide scar area and mean

686 values of stress proxies of (a) failure potential at 500 m below the surface, (b) the

687 depth at which the least compressive stress = 10 MPa, and **(c)** least compressive stress
688 at 500 m below surface, topographic metrics of **(d)** topographic gradient (%), **(e)** local
689 relief, **(f)** elevation, **(g)** distance to channel, and **(h)** mean negative curvature, and
690 seismic shaking proxies of **(i)** peak ground acceleration (PGA), **(j)** curvature-
691 corrected PGA, and **(k)** distance to fault, and precipitation proxies of **(l)** mean annual
692 precipitation rate, **(m)** 90th percentiles of precipitation magnitude, and **(n)** slope
693 instability proxy (SIP). The explanation for the symbols, colors, and lines are the
694 same as Fig. 2.
695
696

697



698

699

700 **Supplementary Figure 8.** Comparison between landslide areal density and (a) the

701 95th and (b) 50th percentile of landslide scar areas and between (c) the 50th and 95th

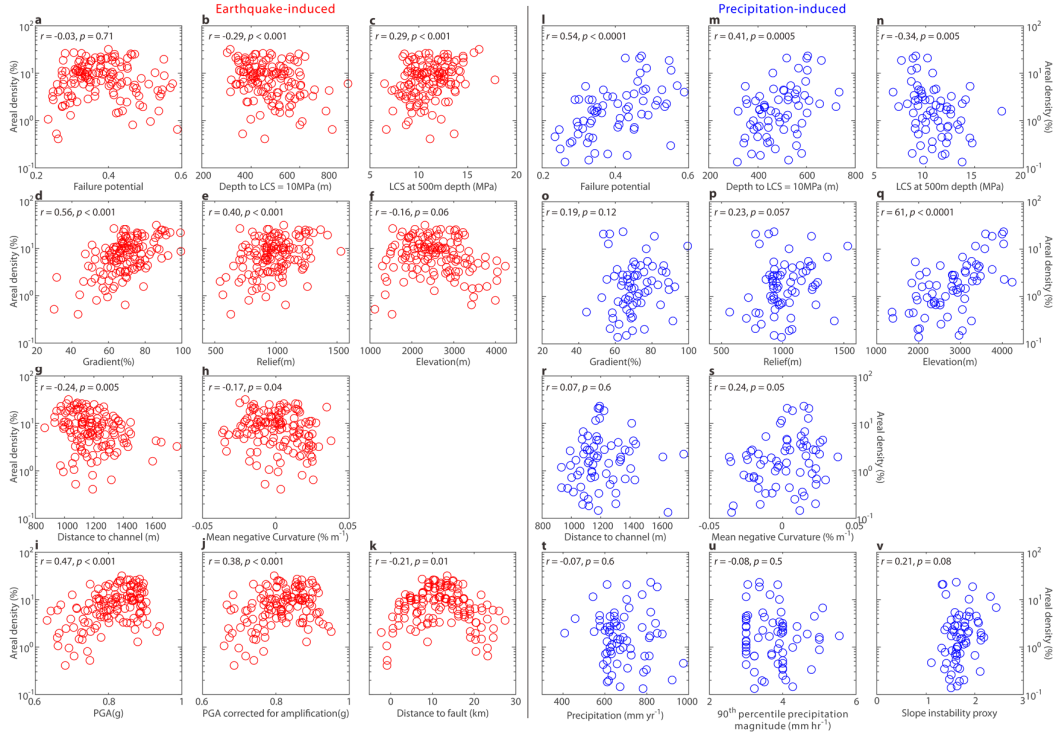
702 percentiles of landslide scar area from the grid-based analysis. There are positive

703 relationships among areal density of landslides and the 50th and 95th percentiles of

704 landslide scar areas, but there is still appreciable scatter within the data.

705

706



708

709

710 **Supplementary Figure 9.** Comparison between areal density of **(a-k)** earthquake-

711 induced and **(l-w)** bedrock landslides and stress proxies of **(a, l)** failure potential at

712 500 m below the surface, **(b, m)** the depth at which the least compressive stress = 10

713 MPa, and **(c, n)** least compressive stress at 500 m below surface. Areal density from

714 both landslide types were also compared with topographic metrics of **(d, o)**

715 topographic gradient (%), **(e, p)** local relief, **(f)** elevation, **(g)** distance to channel, and

716 **(h)** mean negative curvature. We then compare areal density with seismic shaking

717 proxies of **(i)** peak ground acceleration (PGA), **(j)** PGA corrected for amplification,

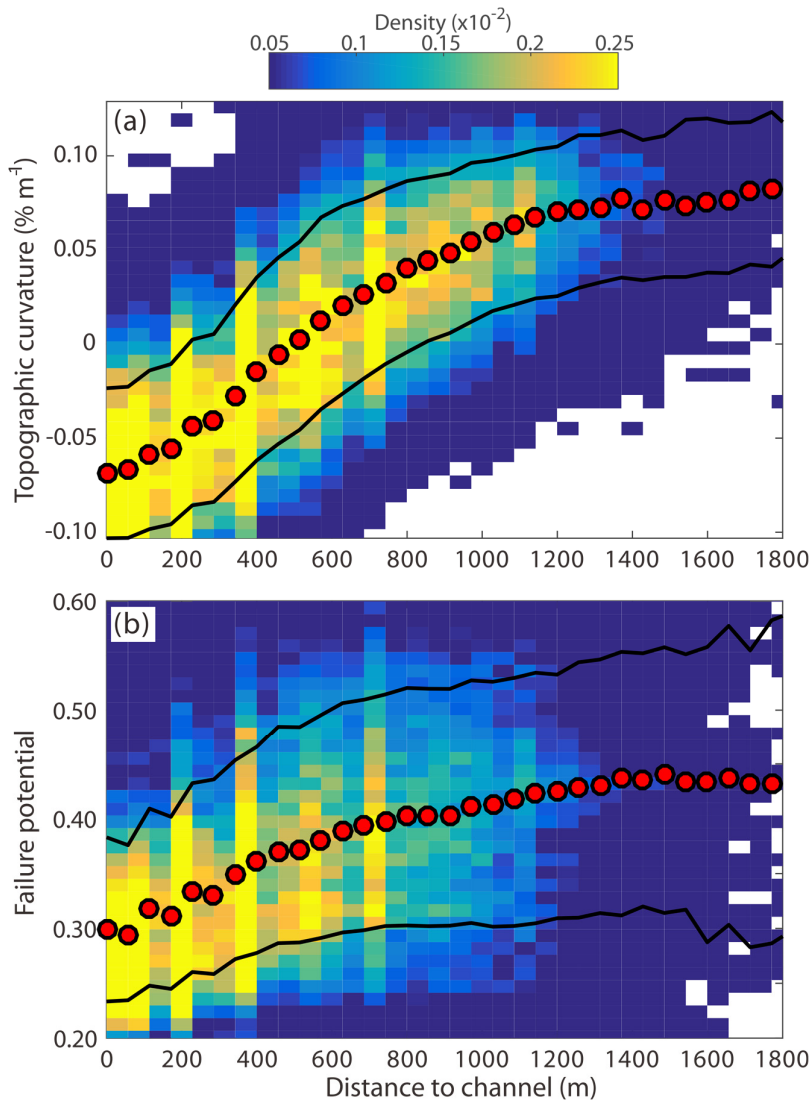
718 and **(k)** distance to fault. Lastly, areal density was compared with precipitation-related

719 proxies of **(t)** mean annual precipitation rate, **(v)** 90th percentiles of precipitation

720 magnitude, and (**w**) slope instability proxy. The explanation for the symbols, colors,

721 and lines are the same as Fig. 2.

722



724

725 **Supplementary Figure 10.** Comparison between distance to channel and (a)

726 topographic curvature and (b) failure potential. Circles indicate the mean values of

727 data points in each bin, and solid black lines represent the 16th and 84th percentiles.

728 The color of the heatmap corresponds to the density of data points (defined as the

729 number of data points in the bin over the total number of data points) for a given bin.

730 Note that the high densities of certain distances are due to the distance to channel

731 incremented by the distance between DEM cells (e.g., 90 m or 126 m).

732 **References**

- 733 1 Roback, K. *et al.* The size, distribution, and mobility of landslides caused by
734 the 2015 Mw7.8 Gorkha earthquake, Nepal. *Geomorphology* **301**, 121-138,
735 doi:10.1016/j.geomorph.2017.01.030 (2018).
- 736 2 Parker, R. N. *et al.* Mass wasting triggered by the 2008 Wenchuan
737 earthquake is greater than orogenic growth. *Nat Geosci* **4**, 449-452,
738 doi:10.1038/Ngeo1154 (2011).
- 739 3 Whadcoat, S., Kathleen. *Landsliding and sediment dynamics following the*
740 *2008 Wenchuan Earthquake in the Beichuan area of China* Master thesis,
741 Durham University, (2011).
- 742 4 Li, G. *et al.* Earthquakes drive focused denudation along a tectonically active
743 mountain front. *Earth and Planetary Science Letters* **472**, 253-265,
744 doi:https://doi.org/10.1016/j.epsl.2017.04.040 (2017).
- 745 5 Larsen, I. J. & Montgomery, D. R. Landslide erosion coupled to tectonics and
746 river incision. *Nat Geosci* **5**, 468-473, doi:10.1038/ngeo1479 (2012).
- 747 6 Huang, D., Li, Y. Q., Song, Y. X., Xu, Q. & Pei, X. J. Insights into the
748 catastrophic Xinmo rock avalanche in Maoxian county, China: Combined
749 effects of historical earthquakes and landslide amplification. *Engineering*
750 *Geology* **258**, 105158, doi:10.1016/j.enggeo.2019.105158 (2019).
- 751 7 Pei, X.-j. *et al.* On the initiation, movement and deposition of a large
752 landslide in Maoxian County, China. *J. Mt. Sci.* **15**, 1319-1330,
753 doi:10.1007/s11629-017-4627-1 (2018).

- 754 8 Marc, O., Meunier, P. & Hovius, N. Prediction of the area affected by
755 earthquake-induced landsliding based on seismological parameters. *Nat.*
756 *Hazards Earth Syst. Sci.* **17**, 1159-1175, doi:10.5194/nhess-17-1159-2017
757 (2017).
- 758 9 Meunier, P., Hovius, N. & Haines, A. J. Regional patterns of earthquake-
759 triggered landslides and their relation to ground motion. *Geophysical*
760 *Research Letters* **34**, doi:10.1029/2007gl031337 (2007).
- 761 10 Ren, J. *et al.* Surface rupture of the 1933 M 7.5 Diexi earthquake in eastern
762 Tibet: implications for seismogenic tectonics. *Geophys J Int* **212**, 1627-1644,
763 doi:10.1093/gji/ggx498 (2017).
- 764 11 Gorum, T. *et al.* Distribution pattern of earthquake-induced landslides
765 triggered by the 12 May 2008 Wenchuan earthquake. *Geomorphology* **133**,
766 152-167, doi:10.1016/j.geomorph.2010.12.030 (2011).
- 767 12 Xu, C., Xu, X., Yao, X. & Dai, F. Three (nearly) complete inventories of
768 landslides triggered by the May 12, 2008 Wenchuan Mw 7.9 earthquake of
769 China and their spatial distribution statistical analysis. *Landslides* **11**, 441-
770 461, doi:10.1007/s10346-013-0404-6 (2014).
- 771 13 Dai, F. C. *et al.* Spatial distribution of landslides triggered by the 2008 Ms
772 8.0 Wenchuan earthquake, China. *J Asian Earth Sci* **40**, 883-895,
773 doi:10.1016/j.jseaes.2010.04.010 (2011).
- 774 14 Montgomery, D. R. Slope distributions, threshold hillslopes, and steady-state
775 topography. *American Journal of Science* **301**, 432-454, doi:DOI

776 10.2475/ajs.301.4-5.432 (2001).

777 15 Larsen, I. J., Montgomery, D. R. & Korup, O. Landslide erosion caused by
778 hillslope material. *Nat Geosci* **3**, doi:10.1038/ngeo776 (2010).

779 16 Prancevic, J. P., Lamb, M. P., McArdell, B. W., Rickli, C. & Kirchner, J. W.
780 Decreasing landslide erosion on steeper slopes in soil-mantled landscapes.
781 *Geophysical Research Letters* **47**, e2020GL087505,
782 doi:10.1029/2020GL087505 (2020).

783 17 Zhang, J.-W. *et al.* Lithium and its isotopes behavior during incipient
784 weathering of granite in the eastern Tibetan Plateau, China. *Chemical*
785 *Geology* **559**, 119969, doi:10.1016/j.chemgeo.2020.119969 (2021).

786 18 Malamud, B. D., Turcotte, D. L., Guzzetti, F. & Reichenbach, P. Landslide
787 inventories and their statistical properties. *Earth Surface Processes and*
788 *Landforms* **29**, 687-711, doi:Doi 10.1002/Esq.1064 (2004).

789 19 Meunier, P., Hovius, N. & Haines, J. A. Topographic site effects and the
790 location of earthquake induced landslides. *Earth and Planetary Science*
791 *Letters* **275**, 221-232, doi:DOI 10.1016/j.epsl.2008.07.020 (2008).

792 20 Li, G. Connectivity of earthquake-triggered landslides with the fluvial
793 network: implications for landslide sediment transport after the 2008
794 Wenchuan earthquake. *J. Geophys. Res. Earth Surf.* **121**,
795 doi:10.1002/2015jf003718 (2016).

796 21 St. Clair, J. *et al.* Geophysical imaging reveals topographic stress control of
797 bedrock weathering. *Science* **350**, 534-538, doi:10.1126/science.aab2210

798 (2015).

799 22 Iverson, R. M. & Reid, M. E. Gravity-driven groundwater flow and slope
800 failure potential: 1. Elastic Effective-Stress Model. *Water Resour Res* **28**,
801 925-938, doi:10.1029/91wr02694 (1992).

802 23 Martel, S. J. Modeling Elastic Stresses in Long Ridges with the Displacement
803 Discontinuity Method. *pure and applied geophysics* **157**, 1039-1057,
804 doi:10.1007/s000240050016 (2000).

805 24 Martel, S. J. & Muller, J. R. A Two-dimensional Boundary Element Method
806 for Calculating Elastic Gravitational Stresses in Slopes. *pure and applied*
807 *geophysics* **157**, 989-1007, doi:10.1007/s000240050014 (2000).

808 25 Slim, M., Perron, J. T., Martel, S. J. & Singha, K. Topographic stress and
809 rock fracture: a two-dimensional numerical model for arbitrary topography
810 and preliminary comparison with borehole observations. *Earth Surface*
811 *Processes and Landforms* **40**, 512-529, doi:10.1002/esp.3646 (2015).

812 26 Thomas, A. L. *Poly3D: A three-dimensional, polygonal element,*
813 *displacement discontinuity boundary element computer program with*
814 *applications to fractures, faults, and cavities in the earth's crust* Master
815 thesis, Stanford University, (1993).

816 27 Moon, S., Perron, J. T., Martel, S. J., Holbrook, W. S. & St. Clair, J. A model
817 of three-dimensional topographic stresses with implications for bedrock
818 fractures, surface processes, and landscape evolution. *Journal of Geophysical*
819 *Research: Earth Surface* **122**, 823-846, doi:10.1002/2016jf004155 (2017).

- 820 28 Moon, S. *et al.* Present-day stress field influences bedrock fracture openness
821 deep into the subsurface. *Geophysical Research Letters* **47**, e2020GL090581,
822 doi:10.1029/2020GL090581 (2020).
- 823 29 Wu, M. *et al.* Preliminary results of in-situ stress measurements along the
824 Longmenshan Fault zone after the Wenchuan Ms 8.0 earthquake. *Acta*
825 *Geologica Sinica - English Edition* **83**, 746-753, doi:10.1111/j.1755-
826 6724.2009.00098.x (2009).
- 827 30 Wang, C., Song, C., Guo, Q., Mao, J. & Zhang, Y. New insights into stress
828 changes before and after the Wenchuan Earthquake using hydraulic
829 fracturing measurements. *Engineering Geology* **194**, 98-113,
830 doi:10.1016/j.enggeo.2015.05.016 (2015).
- 831 31 Meng, W. *et al.* Characteristics and implications of the stress state in the
832 Longmen Shan fault zone, eastern margin of the Tibetan Plateau.
833 *Tectonophysics* **656**, 1-19, doi:10.1016/j.tecto.2015.04.010 (2015).
- 834 32 Heidbach, O., Rajabi, M., Reiter, K., Ziegler, M. & Team, W. (ed GFZ
835 Data Services.) (2016).
- 836 33 Miller, D. J. & Dunne, T. Topographic perturbations of regional stresses and
837 consequent bedrock fracturing. *Journal of Geophysical Research: Solid*
838 *Earth* **101**, 25523-25536, doi:10.1029/96jb02531 (1996).
- 839 34 Brenguier, F. *et al.* Postseismic relaxation along the San Andreas fault at
840 Parkfield from continuous seismological observations. *Science* **321**, 1478-
841 1481, doi:10.1126/science.1160943 (2008).

- 842 35 Hardebeck, J. L. & Okada, T. Temporal stress changes caused by
843 earthquakes: A review. *Journal of Geophysical Research: Solid Earth* **123**,
844 1350-1365, doi:10.1002/2017JB014617 (2018).
- 845 36 Kirby, E., Whipple, K. X., Tang, W. & Chen, Z. Distribution of active rock
846 uplift along the eastern margin of the Tibetan Plateau: Inferences from
847 bedrock channel longitudinal profiles. *Journal of Geophysical Research:*
848 *Solid Earth* **108**, n/a-n/a, doi:10.1029/2001jb000861 (2003).
- 849 37 Maufroy, E., Cotton, F., Cruz - Atienza, V. M. & Gaffet, S. Frequency-
850 scaled curvature as a proxy for topographic site-effect amplification and
851 ground motion variability. *Bulletin of the Seismological Society of America*
852 **105**, 354-367, doi:10.1785/0120140089 (2015).
- 853 38 Rault, C. *et al.* Seismic response of a mountain ridge prone to landsliding.
854 *Bulletin of the Seismological Society of America* **110**, 3004-3020,
855 doi:10.1785/0120190127 (2020).
- 856 39 Xu, Y. *et al.* S-wave velocity structure of the Longmen Shan and Wenchuan
857 earthquake area. *Chinese Journal of Geophysics (in Chinese with English*
858 *abstract)* **52**, 329-338 (2009).
- 859 40 Kirkpatrick, H. M., Moon, S., Yin, A. & Harrison, T. M. Impact of fault
860 damage on eastern Tibet topography. *Geology*, doi:10.1130/g48179.1 (2020).
- 861 41 Bookhagen, B. & Burbank, D. W. Toward a complete Himalayan
862 hydrological budget: Spatiotemporal distribution of snowmelt and rainfall
863 and their impact on river discharge. *Journal of Geophysical Research* **115**,

864 doi:10.1029/2009jf001426 (2010).

865 42 Montgomery, D. R. & Dietrich, W. E. A physically based model for the
866 topographic control on shallow landsliding. *Water Resour Res* **30**, 1153-
867 1171, doi:10.1029/93wr02979 (1994).

868 43 Günther, A., Carstensen, A. & Pohl, W. Automated sliding susceptibility
869 mapping of rock slopes. *Nat. Hazards Earth Syst. Sci.* **4**, 95-102,
870 doi:10.5194/nhess-4-95-2004 (2004).

871 44 Moon, S. *et al.* Climatic control of denudation in the deglaciated landscape of
872 the Washington Cascades. *Nature Geosci* **4**, 469-473, doi:10.1038/ngeo1159
873 (2011).

874